Journal of Nuclear Materials 603 (2025) 155408

Contents lists available at ScienceDirect

Journal of Nuclear Materials

journal homepage: www.elsevier.com/locate/jnucmat

Exploring W-EUROFER brazed joints: S/TEM and nanoindentation analysis following post-brazing tempering treatment

I. Izaguirre [a,*], M. Roldán [b], J. de Prado [a], V. Bonache [a], M. Sánchez [a,c], A. Ureña [a,c]

[a] Materials Science and Engineering Area, ESCET, Universidad Rey Juan Carlos, C/Tulipán s/n, Móstoles, Madrid 28933, Spain
[b] Division of Fusion Technologies, National Fusion Laboratory, CIEMAT, Avenida Complutense, 40, Madrid, Spain
[c] Instituto de Tecnologías Para la Sostenibilidad, Universidad Rey Juan Carlos, C/ Tulipán s/n, Móstoles, Madrid 28933, Spain

HIGHLIGHTS

- Stress relief at the joint interface occurred during tempering, resulting in reduced mechanical properties across various materials and phases within the joint.
- Critical precipitates unique to EUROFER, remained unaffected, with slightly enlarged grain sizes observed farther from the joint.
- Copper's mechanical properties remained largely unaffected by tempering, indicating its capacity for stress accommodation through plastic deformation.
- Design considerations must account for the decrease in EUROFER's hardness and modulus post-tempering to ensure joint longevity and reliability.

ARTICLE INFO

Keywords:
EUROFER
Tungsten
Copper
Fusion reactor
Interfacial characterization

ABSTRACT

Tempering treatments are essential for restoring the hardness and microstructure of EUROFER steel when W-EUROFER joints are formed at temperatures exceeding the steel's austenitization point (890 °C). This post-brazing heat treatment can, however, alter the microstructure and thereby affect the mechanical properties. This study explores the microstructural and nanomechanical effects in the brazed area of W-EUROFER joints following this heat treatment, utilizing copper as an intermediate filler material. Using Scanning Transmission Electron Microscopy (STEM) with Energy Dispersive Spectroscopy (EDS) on FIB lamellae and nanoindentation techniques we examined the stability and phase characteristics of the post-tempered microstructure in two lamellae that covers the whole phases of the braze microstructure.

The tempering process enhances copper diffusion and the growth of copper precipitates without significantly altering the joint's overall microstructure. Despite the general stress-relief effects of tempering, which typically lower mechanical properties, the diffusion phases formed during brazing maintained high hardness and modulus, indicative of a complex, element-rich composition. A reduction in mechanical properties was observed in the iron-rich phase near the W-braze interface and the EUROFER base material, aligning with the purpose of the heat treatment. However, the copper braze and tungsten base material largely retained their stability and resilience to thermal treatments.

This research provides vital insights into the behavior of these material systems under thermal processing, highlighting the necessity of optimizing heat treatment parameters to preserve joint integrity in high-performance applications such as nuclear fusion reactors. The findings contribute significantly to the development of durable and reliable materials for fusion energy, emphasizing the importance of controlled tempering processes to enhance material properties.

1. Introduction

The development of a practical, safe, and reliable source of nuclear fusion energy has been a long-standing goal for the scientific community. One of the most promising solutions to this challenge is the development of a DEMOnstration fusion reactor (DEMO), which aims to produce more energy than it consumes, offering a nearly inexhaustible source of clean and sustainable energy [1,2].

* Corresponding author.
E-mail address: ignacio.izaguirre@urjc.es (I. Izaguirre).

https://doi.org/10.1016/j.jnucmat.2024.155408
Received 28 May 2024; Received in revised form 6 September 2024; Accepted 12 September 2024
Available online 13 September 2024

The success of a DEMO would significantly impact energy production, climate change mitigation, and global energy security, offering a virtually limitless source of clean energy without greenhouse gas emissions or radioactive waste. Thus, the development and operation of a DEMO fusion reactor are crucial. Its success would represent a major milestone in sustainable energy pursuit, potentially revolutionizing energy generation [3,4].

Materials for a fusion reactor must withstand high temperatures, intense radiation, and corrosive environments while maintaining mechanical strength and structural integrity. They must also be economically viable and readily available to ensure the fusion power plant's feasibility. Research into metals, ceramics, and composites is ongoing to identify optimal materials for the DEMO fusion reactor [5]. Developing suitable materials is critical for fusion energy's long-term success as a clean, sustainable source.

Tungsten has been identified as a promising material for the DEMO fusion reactor due to its exceptional mechanical strength, high melting point, and excellent erosion and corrosion resistance. Its properties make it ideal for high-temperature environments, like plasma-facing components of a fusion reactor, where it will face extreme temperatures, radiation, and harsh conditions [6,7]. Tungsten's abundance and longevity make it a cost-effective option for fusion power plants. Extensive research aims to enhance tungsten's performance in DEMO reactors and develop high-quality manufacturing techniques. Some examples of such development are the self-passivating tungsten or TiO/Y_2O_3 precipitation hardened tungsten [8].

EUROFER, a Reduced Activated Ferritic Martensitic steel (RAFM steel), has been developed specifically for DEMO reactors, offering high strength, ductility, and radiation damage resistance. As a low-activation steel, EUROFER produces minimal radioactive isotopes under radiation, enhancing fusion plant safety [9,10]. On the other hand, copper has been proposed as a filler material for joining W to EUROFER in DEMO reactors due to its high thermal conductivity and compatibility with fusion reactor materials. It could, also, serves as pipe material in cooling channels for the divertor to efficiently remove heat from the plasma [11]. However, challenges include copper's low melting point and degradation under neutron irradiation [12].

The brazing process, necessary to join several first wall components, influenced by temperature and time, necessitates subsequent heat treatment to achieve desired material properties. Tempering, as a heat treatment process, has been extensively studied for EUROFER, to improve its mechanical properties and resistance to damage making it more resistant to deformation, cracking, and other forms of damage, which is crucial for fusion reactor components [13–15]. It confers the final microstructure and mechanical properties to the steel by modifying the martensite, formed by cooling from the austenitization field at rates higher than 5 °C/min, into tempered martensite and producing a stress relief effect enhancing the toughness properties of the material [16]. It is commonly assumed that as the tempering temperature increases, the yield strength decreases gradually, while the tensile strength decreases first and then increases. This phenomenon could be associated to the carbide's formation and precipitation typically of the high alloyed steel when applying high temperatures tempering process.

It is then necessary, then, to study the influence, in the brazed joint, of the application of the post brazing heat treatment (EUROFER tempering process). This tempering treatment do not reach the melting of filler alloy, carefully selected for that purpose, but it could promote microstructural modifications that could affect the subsequent service behavior such as diffusion phenomena, phase transformation, phase precipitations…

S/TEM techniques allow detailed evaluation of joints' micro/nanostructure, including phases, grain distribution, and dislocation density. This approach has been supported by high-resolution imaging and analysis of nanostructured coatings and RAFM EUROFER steel, identifying various precipitates and inclusions [17,18]. Furthermore, this technique has been widely used to characterize the effect of tempering on materials [19,20]. In addition, the use of nanoindentation technique has been used for the characterization of both joints and the effects of heat treatments on mechanical properties [21–23].

This paper aims to study the tempering heat treatment's microstructural and mechanical effects in the braze area of W-EUROFER97 joints, assessing its impact on future fusion reactor applications, building on previous welding studies without tempering [24].

2. Experimental details

2.1. Materials

Two base materials were used for bonding: (i) tungsten from Plansee boasting a purity level exceeding 99.97%; and (ii) a reduced activation ferritic/martensitic steel named EUROFER, featuring a chemical composition (in wt.%) of 0.11C, 8.90Cr, 0.42Mn, 0.19V, 1.10W, 0.14Ta, with Fe serving as the balance [18,19]. The dimensions of both tungsten and EUROFER specimens were standardized to $6 \times 6 \times 4$ mm^3 blocks. A pure copper filler material, supplied by Lucas Milhaupt in strip form and 50 μm in thickness, facilitated the bonding between these base materials.

2.2. Brazing process

Brazing experiments were conducted within a high vacuum furnace (Nabertherm P330) under a residual pressure of 10^{-6} mbar. Prior to brazing, the exposed surfaces of the base materials were meticulously prepared using 4000-grit silicon carbide paper. The brazing protocol, refined through prior group studies, specified a single cycle at 1135°C, featuring a dwell time of 10 min and heating/cooling rates of 5 °C/min. The sole applied load, roughly 10 N, originated from the EUROFER material's weight that was applied during the process.

A post-brazing heat or tempering treatment (PBTT) was applied at 760 °C for 90 min, aiming to replicate EUROFER's microstructure and mechanical properties. The microstructure and nanomechanical properties of the braze area were then compared to those obtained from samples without the PBTT.

2.3. Characterization techniques

The microstructures were characterized using TEM and STEM using a JEOL JEM 3000F equipped with an EDS INCA microanalysis suite. The STEM's annular dark field detector (ADF) enabled both low angle annular dark field (LAADF) and high angle annular dark field (HAADF) imaging, varying the camera length for optimal contrast.

In focusing on the microstructure, STEM mode was primarily employed, utilizing either LAADF or HAADF imaging to minimize contrast from forest dislocations and clearly visualize precipitates through pure Z-contrast. HRTEM was also leveraged for identifying secondary phases, with lattice images of select precipitates captured along primary zone axes and analyzed via digital diffraction patterns in Gatan Digital Micrograph software. *Crystal Maker* and *Single Crystal* software have been used to perform a tentative analysis of the crystal structure.

Lamella extraction for analysis involved a standard lift-out procedure using a Focus Ion Beam (FIB), whose procedure is shown in Fig. 1 is detailed as follows:

- Initial milling at 16 KV and 21 nA at a 53° inclination to approximately 150 nm thickness.
- Coarse polishing at 5 KV and 16 nA at the same inclination to a thickness nearing 50-60 nm.
- Final polishing at 2 KV and 28 pA, with two passes each at 57° and 47° inclinations for about 2 s each.

Two lamellae representing the braze microstructure were extracted

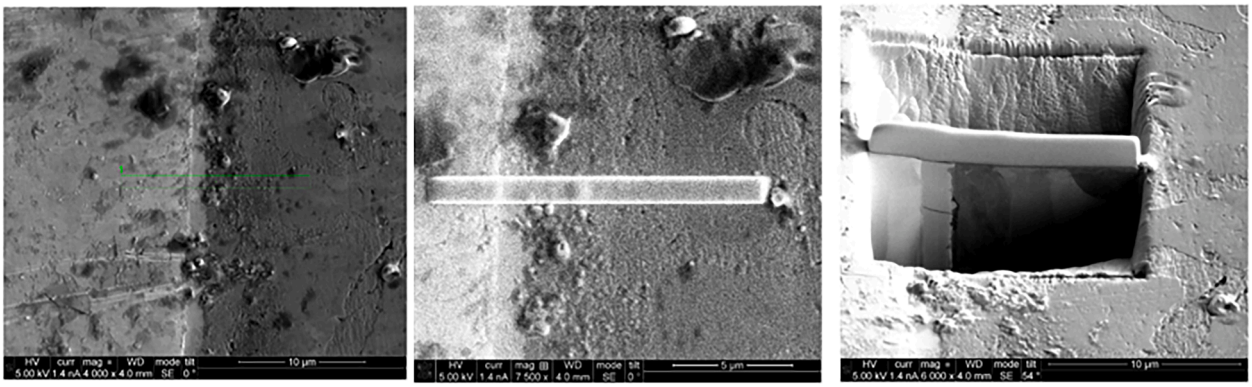

Fig. 1. Lif-out extracting process of the lamella from the W-Cu interface.

from the braze zone. The exact positions of the lamellae extraction were carefully selected to cover all phases that constitute the braze, as it is later discussed in Fig. 2.

Nanoindentation was employed to evaluate the mechanical properties, using a pyramidal Berkovich tip alongside Continuous Stiffness Measurement Control (CSM). This setup allowed for real-time hardness and elastic modulus measurements during indentation, with data collected up to a 150 nm penetration depth and a 5 nm harmonic oscillation amplitude.

Indentation results provided continuous nanohardness (H) and nanoindentation modulus (E) values as a function of penetration depth, with average nanohardness and nanoindentation modulus values considered for analysis within the 100 to 120 nm range. To thoroughly assess all phases in the braze, multiple indentation lines intersected both interfaces at a shallow angle.

3. Results

3.1. Microstructural characterization

Fig. 2 provides an overview of the microstructure of the braze area following the tempering treatment and the position of the lamella extracted from the braze area. Taking into account the thickness of the interest zone two lamella were extracted to cover all phases of the braze area, marked in Fig. 2, the first one of the W-braze interface and the second one of the Cu-EUROFER interface. The overall view of the braze area does not show significant changes compared to the sample without tempering, studied in [24], due to the specific temperature and time conditions of the treatment. The overall microstructure is comprised of the tungsten base material, in contact with a diffusion layer approximately 2-3 μm thick (phase I). This is followed by a phase rich in iron (phase II). The formation of this phase, between the copper braze and the tungsten base material, is associated with a partial dilution of iron during the brazing process, helped by the increased of iron solubility in copper at the brazing temperatures. Then, as the cooling stage reduces the system temperature, the solubility starts to decrease and iron precipitates in contact with the diffusion layer forming this rich phase. On top of this Fe-rich phase, a copper band (phase III) is observed. The conditions of brazing facilitated the penetration of molten copper into the austenitic grain boundaries (phase IV) of the EUROFER base material.

Fig. 3a illustrates the reconstruction of lamella 1 using several STEM and TEM micrographs, which analyses the W-braze interface and comprises three of the above-described phases: the diffusion layer, Fe-rich phase and copper band. The study of the copper band reveals the presence of a high dislocation density for two primary reasons: the residual stresses relief produced during the cooling stage of the brazing process associated with the mismatch in the Coefficient of Thermal Expansion (CTE). This relief occurred mainly during the PBTT and the copper's inherent ability to relieve stresses through plastic deformation. These observations are shown in Fig. 3. Fig. 3c presents a micrograph obtained via STEM, showing the interface between the Fe-rich phase and Cu. A high density of dislocations is observed at the Cu grain boundaries (as these dislocations appear white when taken at a medium angle in ADF), whereas Fig. 3b shows a micrograph, also from the same interface but taken in TEM mode that highlights the contrast difference between the phases. The area shown in blue in Fig. 3b corresponds to the region magnified in Fig. 4a, providing a more detailed visualization of the microstructural features and deeper discussed in the following Figure. Additionally, the characteristic diffraction contrast of TEM is utilized,

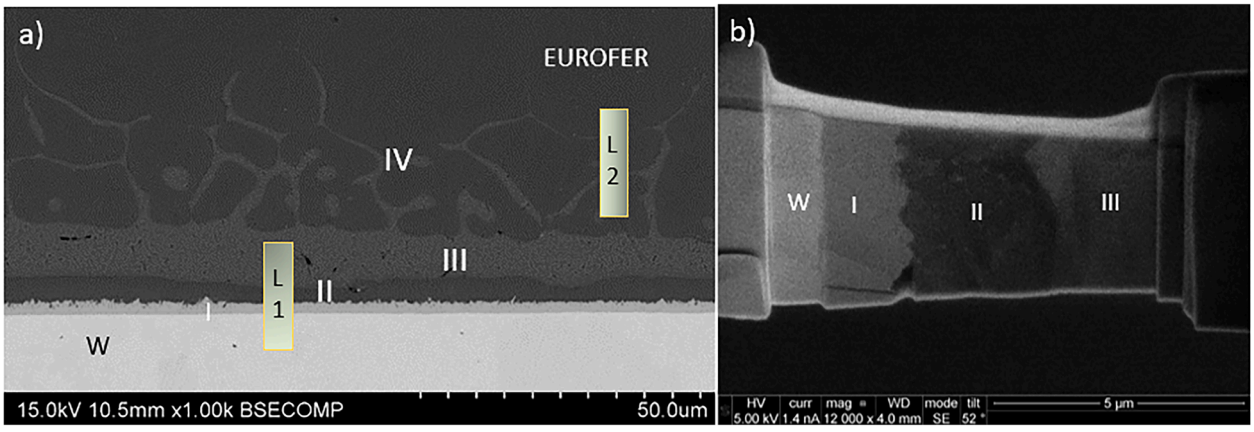

Fig. 2. (a) SEM micrograph of the W-EUROFER brazed joint with all phases presented as diffusion phase (I), iron rich phase (II), copper band (III), and molten copper into austenitic grain boundary (IV), highlighting the extraction areas for lamellae 1 and 2.(b) Example of extracted lamella 1 with presented phases.

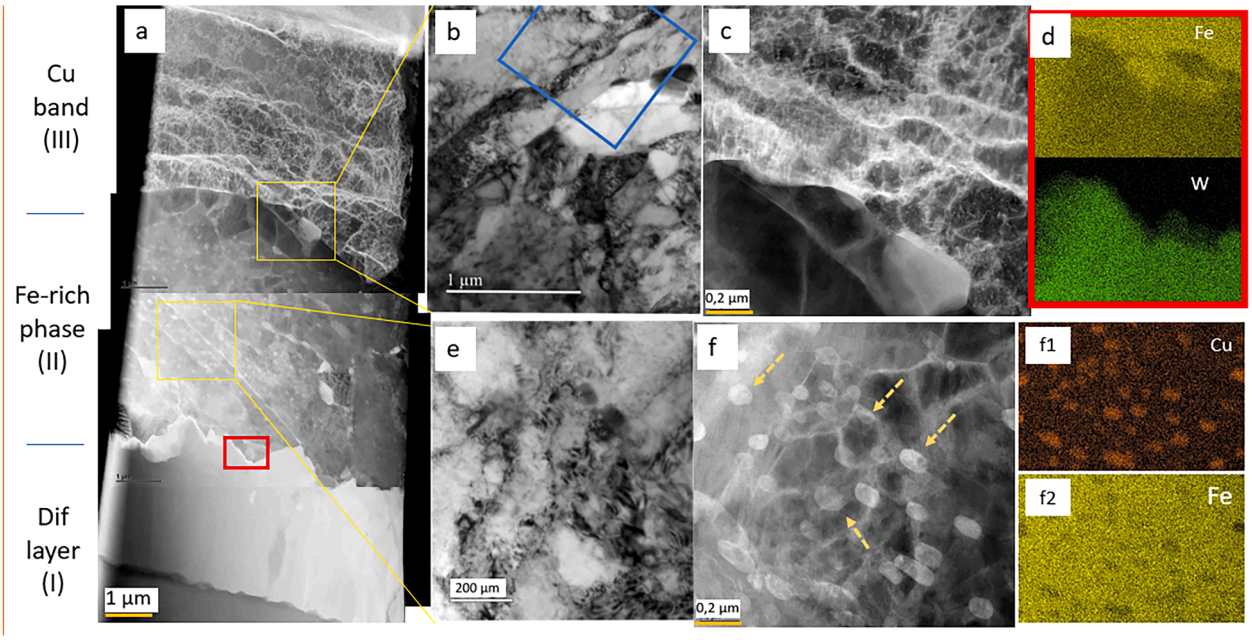

Fig. 3. Lamella 1 reconstruction using S/TEM with detailed micrographs of the different regions. (a) and (b) shown the interface between the Fe-rich phase and Cu band with STEM and TEM mode, respectively, to emphasize the contrast difference between both and the detection of dislocations at Cu grain boundaries. (c, d) shown TEM AND STEM micrographs of the Fe-rich phase with a high amount of Cu-rich precipitates along with the Fe, Cu EDS mapping (blue square), respectively. Red square illustrates the W and Fe distribution at the diffusion layer-Fe-rich phase interface.

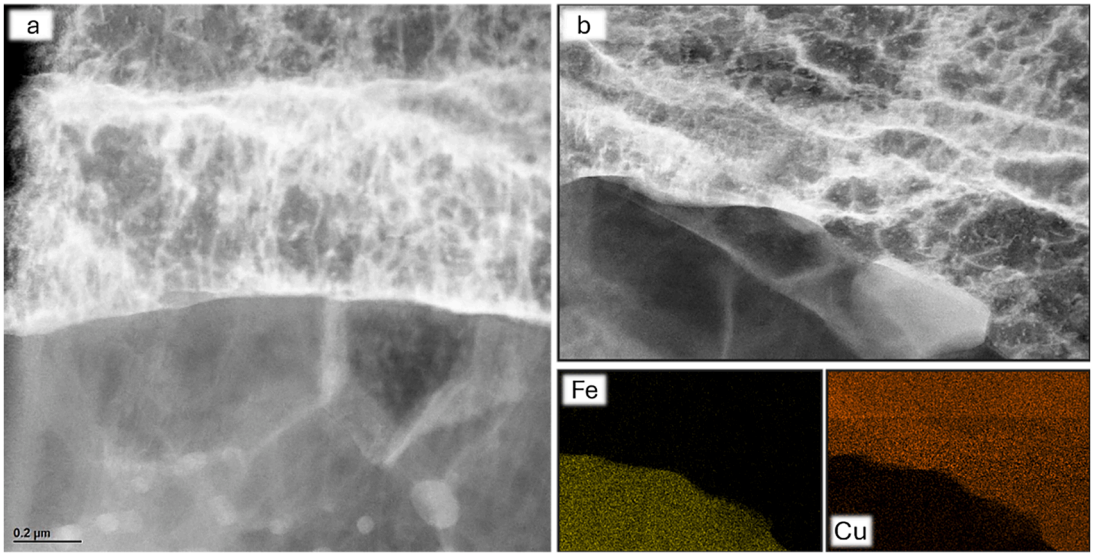

Fig. 4. STEM micrographs with medium angle of ADF showing the high dislocation density in the Cu band (a), and b) includes a chemical mapping of Cu and Fe.

allowing observation of how the Cu band zone is formed by small grains oriented similarly, possibly due to the solidification process following the thermal flow direction.

Fig. 3d is a TEM image of the Fe-rich phase, revealing the presence of a high quantity of Cu-rich precipitates, which formed due to enhanced diffusion during the tempering treatment. Fig. 3e shows the same area in STEM mode, this time eliminating orientation contrast to allow observation of microstructural features with different Z contrasts. The yellow arrows indicate Cu-rich precipitates distributed along the interface. The EDS mapping images shows in Fig. 3f on the right side of the figure illustrate the elemental distribution of Cu and Fe in the analyzed region, highlighting the complex interaction of elements in these areas.

Finally, the W and Fe mapping distribution analyzed and shown in Fig. 3d in the interface between the diffusion layers and the Fe-rich phase (marked in Fig. 3a with a red square) indicated that W presence is mainly limited to the diffusion layer.

The results provide a comprehensive view of the microstructure and phase distribution in the analyzed lamella, demonstrating the influence of tempering treatment on diffusion and precipitate formation in W-EUROFER joints.

Fig. 4a and 4b (top) clearly illustrate the result of the plastic deformation experienced by the copper layer, evidenced by the white lines which correspond to dislocations. These micrographs show the interface between the Cu phase and the Fe-rich phase. Despite using ADF in STEM mode, these dislocations are not detected in the Fe-rich phase. The dislocations accumulate in the former and are pinned at the beginning of the iron phase, as well as at the Cu band elongated subgrains as shown in Fig. 4a. EDS mapping distribution results from the interfacial region

show the signals of Cu and Fe, demonstrating that there is practically no diffusion of these elements into the other phase.

The diffusion layer observed in W-EUROFER brazed joints exhibits unique characteristics that necessitate a detailed examination to understand its microstructural and crystallographic properties. A preliminary analysis of the crystal structure was performed using TEM and a commercial crystallographic analysis software.

The microstructure of the diffusion phase is characterized by fine lamellae or needle-like shape, as shown in the micrographs of Fig. 5a. These lamellae, measuring on the nanometer scale, suggest an anisotropic growth mechanism likely influenced by thermal stresses and the elemental distribution within the solid solution. The lamellar structure indicates a phase formed under conditions of significant diffusion and element migration during the brazing process and the subsequent post-brazing heat treatment. The morphology of the lamellae points to a high degree of strain and stress accommodation, consistent with the presence of elements in solution within the diffusion phase [25].

Fig. 5 also displays three characteristic TEM micrographs that clearly show the lamellar contrast in the diffusion zone, formed by domains with similar orientations. Fig. 5a presents the interface with W, where the orientation of the Cu-rich diffusion phase's lamellae/needles is seen, aligned perpendicularly to the interface. Fig. 5b focuses on the orientations of the needle-like structures, which form clusters depending on their orientation. Each cluster contains a set of needles with a clearly defined orientation. In contrast, Fig. 5c, a TEM micrograph at 60,000x magnification, highlights regions free of needle structures. By using the smallest selected area aperture to illuminate only the bands within a single domain, the corresponding diffraction pattern was obtained (Fig. 5d). Using CrystalMaker and SingleCrystal software, we attempted to fit a pristine Cu structure, but this yielded significant errors. Assuming the presence of elements in solid solution, Fe and W were selected as potential candidates, with one element having a larger ionic radius and the other a smaller one.

By adjusting the phase composition to 80% Cu, 10% Fe, and 10% W (atomic), the diffraction pattern aligns with the modified unit cell parameters: a = 3.0657 Å, b = 3.4437 Å, c = 3.131 Å, α = 79.595°, β = 87.449°, and γ = 84.7°, with a volume of 32.4 $Å^3$. It should be noted that this adjustment does not confirm that the diffusion layer corresponds to a Cu matrix with these elements in solid solution. Rather, under this assumption, it was possible to identify diffraction planes that theoretically should not appear, suggesting a tentative composition of Cu10W10Fe at%. This result implies that the band may contain Fe and W within the copper matrix, or other similar elements such as Cr, Ta, or V. This could explain the presence of diffraction points for planes that theoretically should not exist in a pure FCC Cu structure, especially considering that the new dimensions result in a triclinic geometry. Assuming the structure is not pure Cu, the diffraction pattern of the diffusion phase aligns with the [1 $\bar{1}$ $\bar{0}$] zone axis.

Once the orientation was determined, the atomic arrangement for the assumed composition was represented along the same zone axis, showing several unit cells and the relationship between the elements in solution. Fig. 5d and 5e illustrate the atomic arrangement along this axis and its volumetric structure, containing proportional amounts of Fe and W. A cubic structure with 16-unit cells was created, allowing for the representation of a random atomic distribution based on the atomic weight of W and Fe, as assumed in this analysis.

Additionally, streaking phenomena were observed in the diffraction pattern, which may result from the presence of needle-like structures

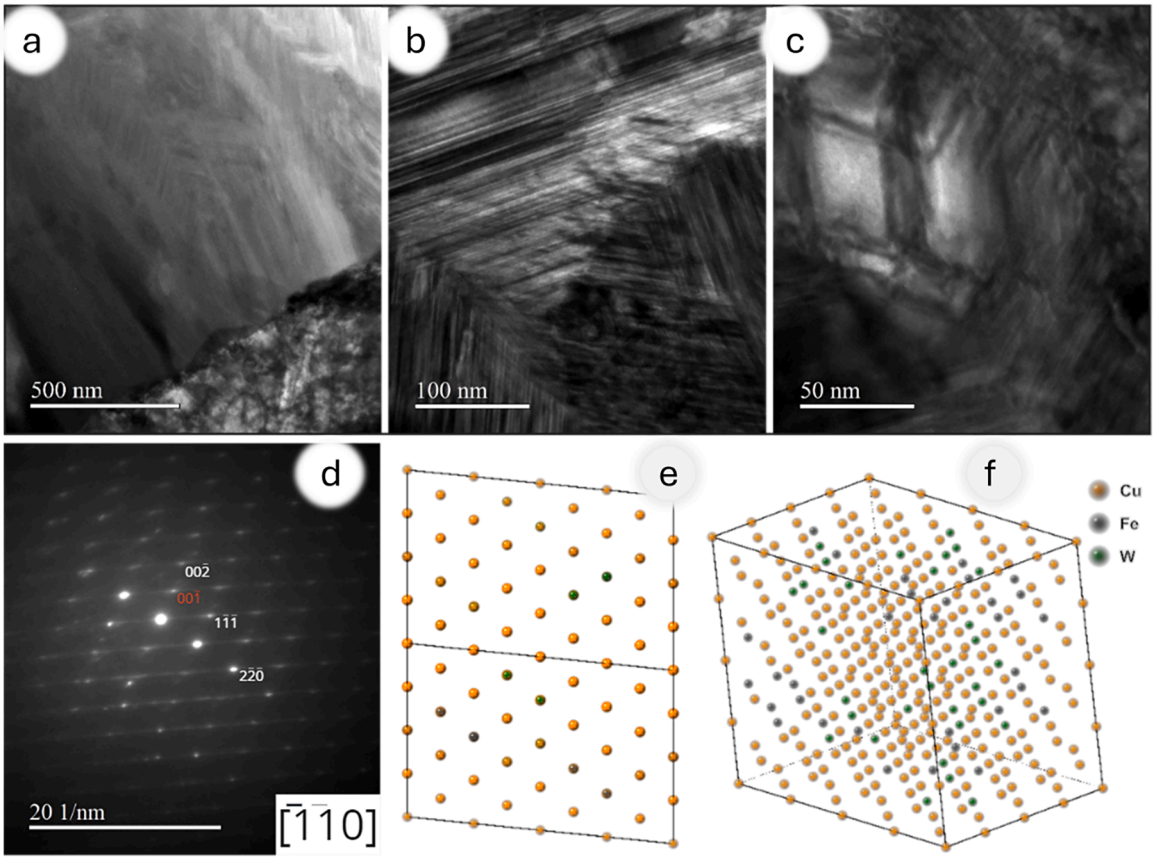

Fig. 5. (a) TEM micrographs at 8 kX showing the interphase between diffusion layer and W, (b) at 30 kX, focusing in the orientations of needle-like structure forming clusters and (c) TEM micrograph at 60 kX highlighting regions free of needle structures, d) TEM diffraction pattern of a needle-like cluster, e)16 unit cells oriented up to [$\bar{1}\bar{1}$0] zone axis (where chemical elements are shown in random positions) and f) crystal structures containing 16 unit cells, illustrating the distribution of the proposed elements (Cu, Fe, and W) within the structure.

with extremely fine grain sizes, similar to those observed in epitaxial growth structures. Less bright points deviating from the primary diffraction pattern likely indicate secondary phase precipitates, which are more diffuse or less defined due to their dispersed nature or reduced volume relative to the primary matrix. It is possible that their nucleation was facilitated by the tempering treatment, which increases atomic mobility and promotes the diffusion of solute atoms. This enhanced diffusion allows elements to migrate more easily within the material, providing the conditions necessary for the formation and growth of secondary phases. The heat treatment may have also relieved internal stresses, creating additional favourable sites for nucleation and facilitating the precipitation of these secondary phases. However, their microstructural characterization exceeds the technological scope of this nuclear fusion welding study, as it is not feasible to conduct a detailed electron diffraction study, not only due to the intensity of the spots in the Cu matrix but also because such particles could not be resolved even in HAADF.

Fig. 6 presents a detailed analysis of the diffraction patterns obtained from various regions of the sample. The transformation of the diffraction pattern image into a pattern coloring was performed, where the intensity of the grayscale image was converted into a discrete color scale ranging from black to red. This method enhances the identification of the bright spot centers since the light distribution follows a Gaussian pattern. Subsequently, the real image and the simulated pattern were superimposed, allowing adjustments to the cell volume and distortions of the lattice parameters a, b, and c and their corresponding angles.

In the same way that the compositional variations in the diffusion phase were analyzed, these analyses do not aim to precisely determine the crystal structure but rather provide an understanding of the compositional variation in the microstructural features nucleated after brazing and tempering. Nonetheless, they are suitable for identifying certain types of precipitates, such as M23C6 (Fig. 6a and b), another M23C6-type precipitate whose diffraction pattern captures the signal from two closely spaced particles (Fig. 6c and d), and the BCC structure of alpha-iron (Fig. 6e and f), in the crystal highlighted in red, where the contrast has significantly increased due to the zone axis orientation factor. These observations support the decision to refer to the iron-rich phase as having a BCC structure in this article, rather than identifying it as EUROFER, since it is not possible to confirm the presence of a martensitic structure without further analysis, which is beyond the scope of this study. The diffraction spots show slight displacements, possibly due to elements in solid solution, similar to what occurs with EUROFER.

The colored diffraction patterns facilitate a better understanding of the elemental and structural intricacies within the material. By accounting for cell volume adjustments, lattice distortions, and incorporating elements into solid solutions (as done for the diffusion phase), these patterns reveal the presence of otherwise unexpected planes. The complex analysis required underscores the intricate nature of the phases formed during the brazing and tempering processes, providing insight into the formation of precipitates like M23C6 and the fundamental BCC structure of iron.

In Fig. 7, an energy dispersive spectroscopy (EDS) analysis is presented, conducted throughout the sample to investigate the variation of alloying elements. The most characteristic spectra were selected for detailed representation. In Fig. 7a, a detailed view of an M23C6-type

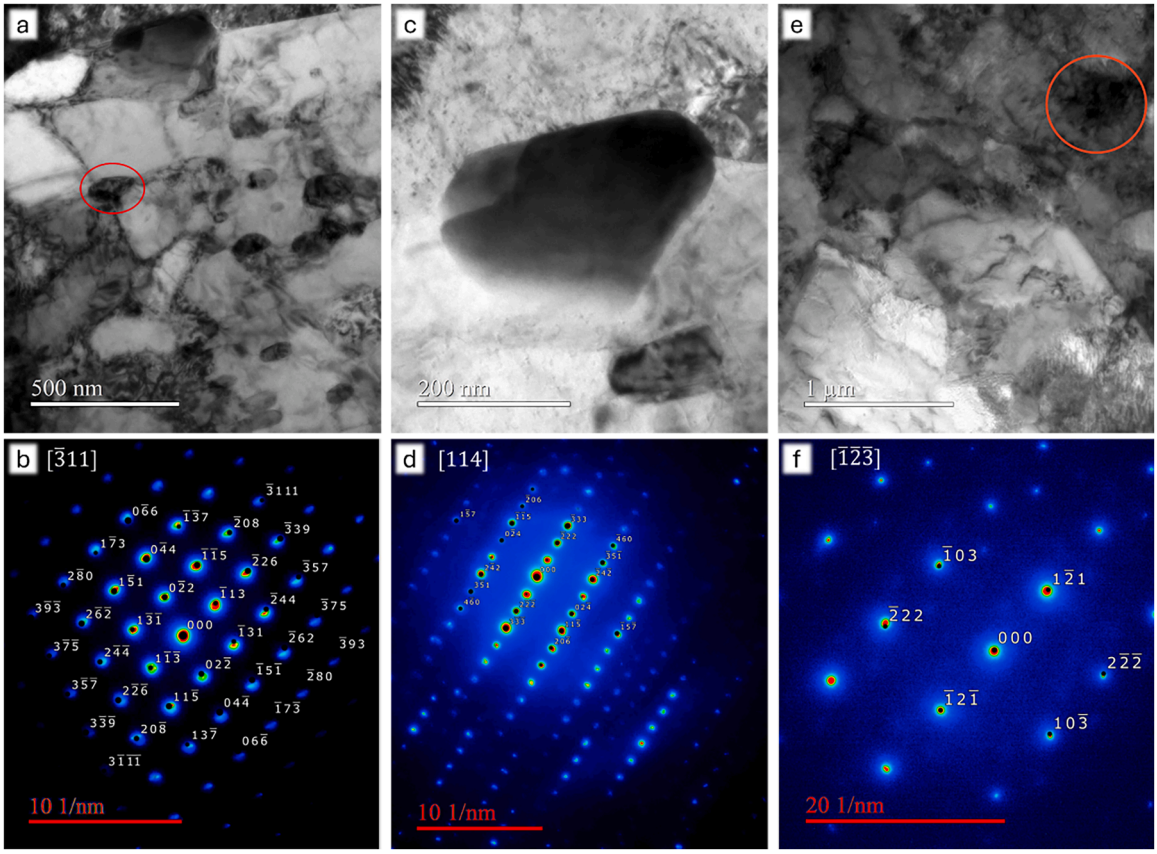

Fig. 6. (a) STEM micrograph showing an M23C6 precipitate within the Fe-rich phase, with the red circle marking the area of interest. (b) Diffraction pattern from the region highlighted in (a), taken along the [311] zone axis. (c) TEM micrograph of another precipitate located in the copper band, illustrating its morphology. (d) Diffraction pattern corresponding to (c), taken along the [114] zone axis, with enhanced coloring to accurately identify bright spots. (e) TEM micrograph of a different area within the Fe-rich phase, with the red circle marking another region of interest. (f) Diffraction pattern from the region highlighted in (e), taken along the [123] zone axis

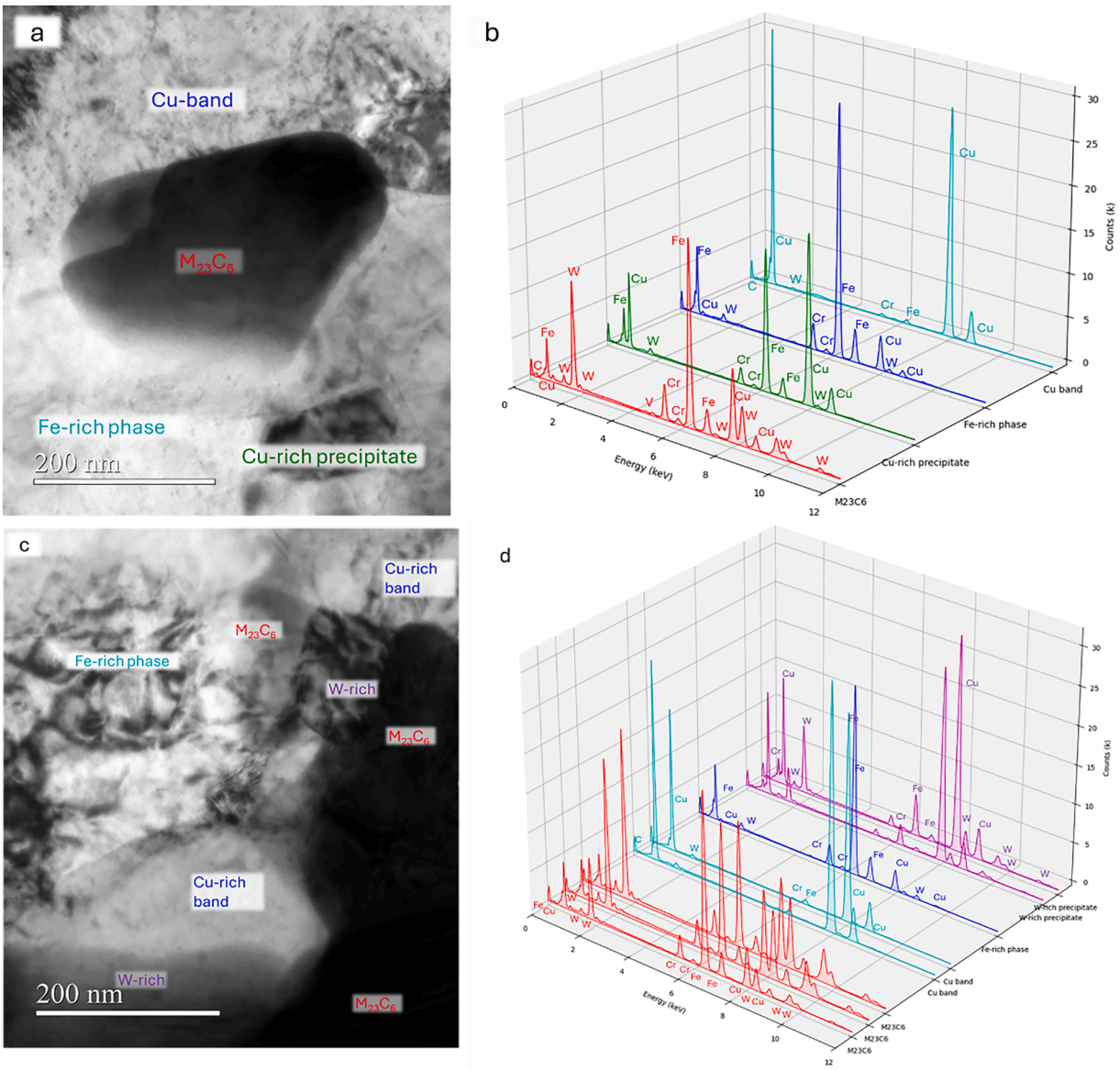

Fig. 7. Details the EDS analysis of the iron-rich phase (a) and the diffusion layer (b), further elucidating the complex interplay of elements within these zones.

precipitate at the interface between the Cu-rich phase and the Fe-rich phase is shown using a TEM micrograph, highlighting the different phases present: Cu-band, Fe-rich phase, and Cu-rich precipitates. In Fig. 7b, the EDS spectra corresponding to image a are displayed, showing the concentrations of Cu, Fe, Cr, and W elements in the different phases. It is revealed that the M23C6 precipitate contains high levels of Cr and W, while the Cu band shows a high concentration of Cu. It demonstrates that a minor quantity of W atoms could be transported during the brazing process up to the Cu band and then interact with other elements to form precipitates. However, as W distribution in Fig. 3 demonstrated, W presence is mainly limited to the diffusion layer [26].

Fig. 7c shows a TEM micrograph of a larger area in the diffusion layer, covering multiple points of analysis and including various phases such as the Cu rich, Fe-rich and W-rich phases, and several M23C6 precipitates. The EDS spectra from the points analyzed in Fig. 7c are shown in Fig. 7d, indicating similar results to those observed in Fig. 7b and demonstrating consistency in the distribution of elements across the different phases. The aim of this analysis was not to precisely characterize the composition and crystalline characteristics of the phases, but rather to perform an initial qualitative descriptive analysis of the distribution of alloying elements in the sample, providing an overall view of how elements are distributed and segregated in the different phases present after the tempering treatment.

The lamella 2, extracted from the interface between copper and EUROFER, depicted in Figs. 8 and 9, shows the nearest zone of EUROFER with the braze area, where the presence of a copper phase penetrating through the austenitic grain boundary divided the base material into two zones. This copper comes from the copper band studied in the previous lamella, which penetrates through those paths, which exhibits a diffusion coefficient several orders of magnitude higher than the bulk grain. It has been reported that the penetration of copper through the steel grain boundary and its combination with Fe and other elements that constitute the steel causes a low liquefaction process in those zones, which explains the observed microstructure [27].

Fig. 8 provides a detailed examination of Lamella 2 using STEM techniques, showcasing different regions at the interface and their elemental compositions. The overall view, presented in the leftmost image, highlights the regions analyzed in more detail in subsequent images. The areas marked in blue and red boxes correspond to the regions magnified in Fig. 8a and b, respectively.

In Fig. 8a, a micrograph obtained via STEM focuses on the upper region of the lamella. The elemental maps adjacent to this micrograph

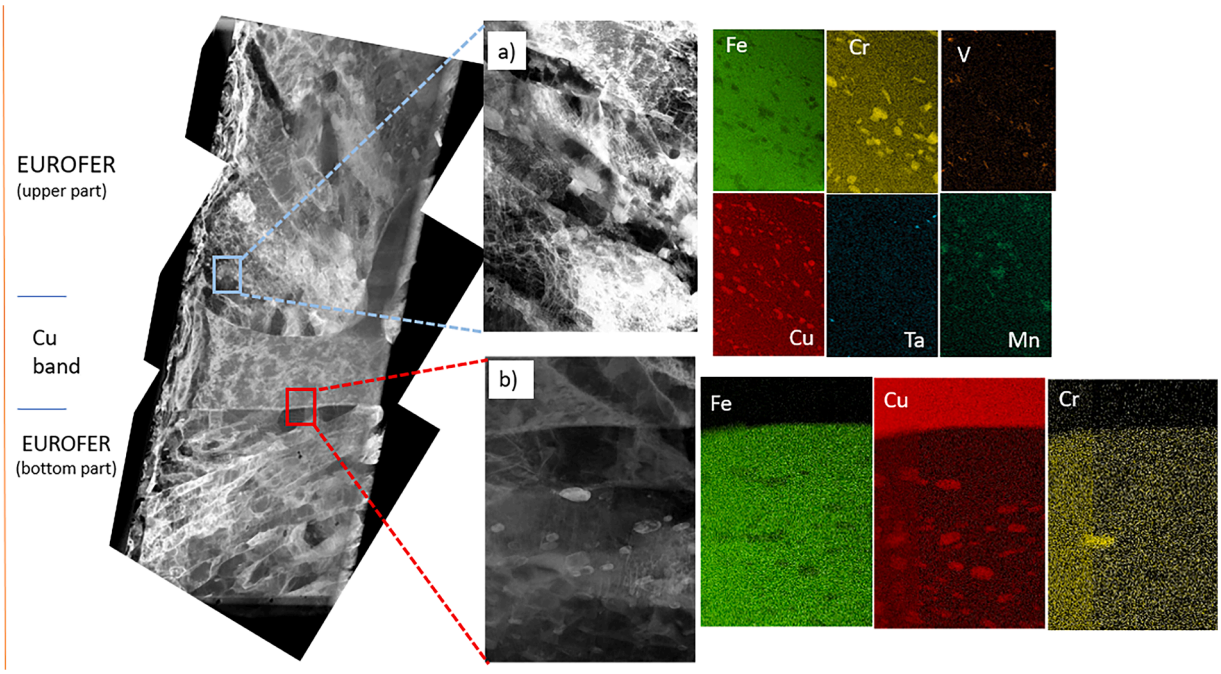

Fig. 8. Reconstructs the second lamella using STEM, providing compositional details of (a) EUROFER upper part and (b) EUROFER bottom part.

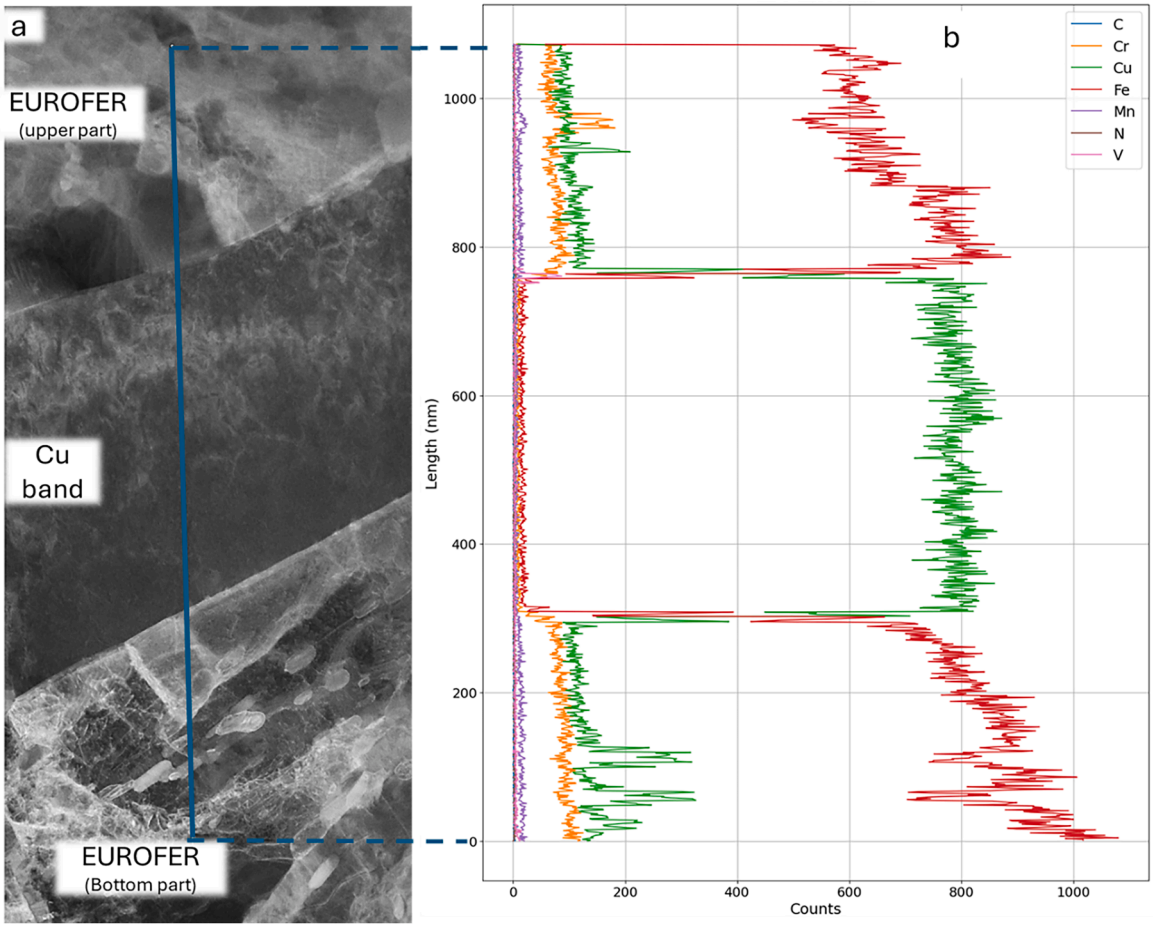

Fig. 9. EDS Line scan across the cu band, offering insights into the interplay of alloying elements at the interfaces, showing very low solution of Cu in EUROFER, only forming secondary particles.

reveal the distribution of several elements including Fe, Cr, V, Cu, Ta, and Mn. The Fe map shows a high concentration of iron, consistent with the Fe-rich phase. Cr and V maps indicate the presence of chromium and vanadium, which are typical alloying elements in EUROFER steel. The Cu map shows the distribution of copper, primarily in the Cu-rich precipitates, while the Ta and Mn maps highlight the distribution of tantalum and manganese.

Fig. 8b, also obtained via STEM, focuses on the lower region of the lamella. The adjacent elemental maps for Fe, Cu, and Cr illustrate the distribution of these elements in this region. The Fe map indicates the presence of the Fe-rich phase, while the Cu map shows copper distribution in the Cu band and the Cr map reveals the presence of chromium. A clear segregation of Fe and Cu, along with the presence of Cr, suggests distinct phase boundaries and the influence of alloying elements on the microstructural stability and mechanical properties of the joint.

The detailed analysis using elemental mapping provides insights into the crystallographic and chemical nature of the diffusion zones. The presence of elements like Ta and Mn, though less concentrated, highlights the intricate alloying and segregation behavior within the brazed joint. The observed microstructural features and elemental distributions are consistent with the enhanced diffusion and precipitate formation caused by the post-brazing tempering treatment, emphasizing the importance of controlled heat treatment processes to optimize the mechanical properties and stability of W-EUROFER joints.

In Fig. 9a, a high-resolution STEM micrograph displays the interface between the Cu band and the EUROFER steel, highlighting both the upper and bottom parts of EUROFER. The presence of a distinct Cu band is evident, indicating a significant diffusion and penetration through grain boundary paths of Cu during the brazing process.

Fig. 9b presents the line scan analysis, showing the elemental distribution across the Cu band and into the EUROFER regions. The green peaks in the Cu line scan are particularly notable, indicating areas of high Cu concentration. These peaks correspond to the locations of Cu-rich precipitates within both the upper and bottom parts of EUROFER.

The line scan data illustrates the limited solubility of Cu in EUROFER steel. Despite this low solubility, Cu has diffused effectively across the interface, forming distinct precipitates. The sharp peaks in the Cu distribution suggest that Cu atoms have migrated and aggregated into precipitates, rather than being uniformly distributed within the EUROFER matrix. This aggregation is consistent with the enhanced diffusion observed during the post-brazing tempering treatment, which facilitates the movement and clustering of Cu atoms into precipitate formations.

The Fe, Cr, and other alloying elements' distributions are also shown, providing a comprehensive view of the elemental interactions within the diffusion zone. The presence of Cr and V, typical alloying elements in EUROFER steel, alongside the Cu precipitates, suggests a complex interaction and segregation behavior influenced by the thermal and diffusion processes during brazing and tempering.

This study complements the previous analysis by providing a quantitative measure of Cu diffusion and its impact on microstructural evolution. The formation of Cu-rich precipitates within the EUROFER steel is a direct result of the diffusion processes facilitated by the post-brazing heat treatment. This behavior highlights the significant role of thermal treatment in altering the microstructural and elemental composition of brazed joints, ensuring the stability and mechanical properties required for high-performance applications such as fusion reactors.

3.2. Mechanical characterization

The results obtained to study the effect of tempering treatment are shown in Fig. 10.

Fig. 11 shows the hardness and nanoindentation modulus profiles of the various phases within the brazed joint after tempering. The white lines indicate the paths of indentation taken across the interfaces to capture the complete mechanical behavior of the joint. The data reveal that the diffusion phase at the interface with tungsten remains the most rigid, while the iron-rich phase and the EUROFER base material show reduced mechanical properties following the tempering. This is significant because it helps avoid creating high-stress areas in weaker phases that could compromise the overall integrity of the joint.

4. Discussion

4.1. Microstructural characterization

In the Fe-rich phase (in Fig. 2), there is a noticeable increase in the size of copper precipitates (arrowed in Fig. 3d) compared to those observed before the tempering heat treatment [24]. This growth is attributed to the process's temperature and duration, which activated the solid-state inter-diffusion phenomena of the elements that constitute the braze. As a result, the presence of copper in the Fe-rich phase is increased resulting in a denser and coarser precipitate formation of approximately 0.13 ± 0.02 microns, versus the 0.08 ± 0.01 microns observed in as-brazed condition [24]. The Fe-rich phase most affected by tempering shows a uniform microstructure constituted of sub-micrometric grains. In the current study, the absence of the

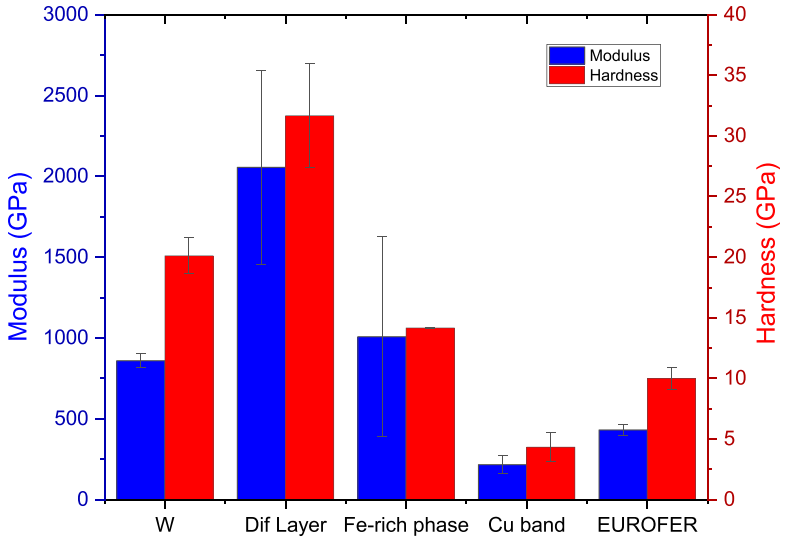

Fig. 10. Hardness and modulus of the phases at the interface after tempering.

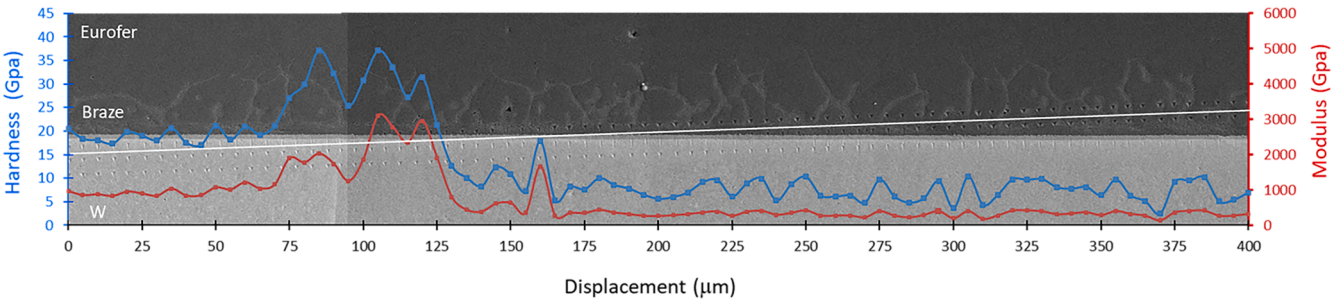

Fig. 11. Hardness (blue) and modulus (red) profiles of the phases that constitute the brazed joint after tempering. The white line refers to the matrix indentation used to get the values.

previously observed martensitic lath, which was noted in prior research on joints that did not undergo the tempering process [24], signifies a novel finding. Moreover, there's a noted reduction in the density of dislocations within this area, which suggests stress relief attributed to the tempering treatment. This qualitative determination of dislocation density reduction, while indicative of the tempering process's efficacy, acknowledges the inherent complexities and potential inaccuracies involved in quantifying dislocation densities, especially in cases of high density and complex morphology. The elemental distribution of Fe and Cu is depicted in Fig. 3d.

Fig. 5 highlights the diffusion layer on the top of the W base material, showing a complex structure. This phase is comprised of several elements, including copper, which presents the same conditions as the case without tempering, with 52W24Fe20Cu4Cr wt. %. The tempering heat treatment enhances the diffusion process, allowing for greater incorporation of copper into this phase despite the typically low solubility between copper and W at operational temperatures, as demonstrated in the binary phase equilibrium diagram [28]. The morphology of this layer microstructure along with a diffraction pattern, is shown in Figs. 5 and 6. The occurrence of spot splitting in diffraction patterns may stem from the existence of needle-like structures with extremely fine grain sizes; such configurations can induce distortions within the crystal lattice arising from internal stresses or the coexistence of multiple phases. Concurrently, the presence of less bright spots that diverge from the primary diffraction pattern could potentially signal the existence of precipitates, these secondary phase formations appearing more diffuse or less defined due to their scattered nature or their reduced volume relative to the principal matrix. Furthermore, the material's texture, inferred through the relative intensity and the spatial arrangement of the diffraction spots, offers insights into the preferential grain orientation. While not directly observable in the diffraction patterns, the density of dislocations and other lattice defects is another factor that can significantly influence the clarity and brightness of the diffraction spots [29]. Discrepancies in the location of the spots from their theoretical positions are indicative of residual stresses within the material's matrix. The granularity of the diffraction pattern also provides clues about the grain size, with a more diffuse pattern generally pointing to finer grains, and a more distinct pattern suggesting larger grains. Additionally, in-plane streaks within the diffraction patterns denote stripe-like domains that are demarcated by grain boundaries or stacking faults, further enriching the microstructural narrative of the material under investigation [30, 31].

A deeper examination of the precipitates and phases detected in the Fe-rich phase and diffusion layer in lamella 1, demonstrates that the tempering significantly enhances the diffusion effect at the interface between the iron-copper rich phase. This is evidenced by the formation of numerous precipitates, including those of copper and others depicted in Fig. 3a. The presence of a precipitate akin to the M23C6 type commonly found in EUROFER steel, characterized by its high chromium and tungsten content, has been detected. Despite fitting the anticipated elemental compositions according to EDS analysis, there is also evidence of iron and copper within the precipitate. Initial thoughts might align with Thermo-Calc software predictions, which foretell the formation of M23C6 carbides at a tempering temperature of 780°C, and STEM observations have indeed confirmed the nucleation of M23C6 on prior austenite grain boundaries as well as on lath or block boundaries, which could potentially incorporate copper [32,33]. Nevertheless, such a copper inclusion lacks precedents in the scientific literature. Hence, by relying on the diffraction pattern (Fig. 6) oriented under zone axis <114> that validates the M23C6 particle type, it is plausible to infer that the presence of iron and copper emanates from the surrounding matrix.

The precipitation reaction is driven by diffusion, with high temperatures facilitating the nucleation and growth of a large number of precipitates at elevated tempering temperatures [34]. Additionally, a copper precipitate, identified in Fig. 7a, with a composition of 57Cu40Fe4Cr wt.%, contains a higher percentage of copper than observed before tempering [24]. This enrichment in copper is due to the tempering temperature, which enhances diffusion, allowing the movement of copper atoms present in the copper band and the precipitates formed after the brazing process. Both precipitates are situated within the Fe-rich phase as indicated by the matrix EDX analysis, in Fig. 7a, with an EDS composition of 77Fe13Cu7Cr3W wt.%. Therefore, this Fe-rich band also has copper, and it is likely that, during the tempering, this phase has been enriched in copper element at the tempering temperature and, the different in solubility between that temperature and room temperature, causes the copper precipitation during the cooling stage.

Fig. 7b showcases several point analyses of the diffusion layer at the interface with tungsten, highlighting its composition of varied elements. This exhaustive characterization reveals the complexity of the phase, consisting of different phases in Fig. 7b with a composition of 52W24Fe20Cu4Cr wt.%, the matrix of the diffusion layer, with 52Fe26W15Cu6Cr wt.%, and with 78Fe11Cu7Cr4W wt.%. These findings indicate a slight change compared to the sample without tempering, as the heat treatment promotes the diffusion of elements to form these compounds, imparting negative properties to the braze interface, for example, under high heat fluxes as spreading cracks or brittleness [35, 36].

The bottom part of EUROFER, closer to the brazed zone, is characterized by the presence of coarsen copper precipitates compared to the upper zone and with the Fe-rich band previously studied (Fig. 8). The sizes of the precipitates are 146 ± 25 nm in the bottom part, versus the 74 ± 13 nm observed in the upper part. The location of this zone, between the Cu band and the Cu phase explained this phenomenon. This is illustrated by the line scan, Fig. 9, which shows an increase in the percentage of copper when scanning through the precipitates, and a decrease in the percentage of other elements. Additionally, the upper zone of EUROFER, which is less affected by the brazed area, exhibits various alloying elements characterized by different precipitates, maintaining the EUROFER characteristic features, like various MX of V and Ta, and some $M_{23}C_6$ of Cr replaced by Mn (Fig. 9b). This indicates

that despite the heat treatment, these critical precipitates are preserved at distances lower than 20 μm from the W-braze interface, showcasing slightly larger grains compared to those nearer the braze area [37,38].

4.2. Mechanical characterization

In the area of nanomechanical characterization, although the tempering treatment aims to relieve the stress and modified the EUROFER microstructure also modified the braze and joint interface properties in the same line. This results in a measurable reduction in the nanomechanical properties of the different materials and phases that constitute the joint. Fig. 10 illustrates this effect, showing that the diffusion phase at the interface with tungsten maintains its high mechanical properties (2055 ± 598 GPa for nanoindentation modulus and 32 ± 4 GPa for nanohardness), thanks to a complex structure that incorporates elements such as W, Cr, and Fe. These properties are consistent with those measured after the brazing process, prior to any tempering [17].

The iron-rich phase exhibits a decrease in mechanical properties due to the tempering, as evidenced by the stress relief seen in earlier sections. The values for this phase are recorded as 1007 ± 618 GPa for nanoindentation modulus and 14.5 ± 0.1 GPa for nanohardness, a decline when compared to the untreated material. In the case of the EUROFER base material, there is a noticeable modification in nanomechanical properties before and after the application of the PBTT, from 450 ± 29 GPa for nanoindentation modulus and 16 ± 1 GPa for hardness to 431 ± 34 GPa for nanoindentation modulus and 10 ± 1 GPa for nanohardness after tempering. This represents a 4.27% decrease in nanoindentation modulus and a more significant 36.88% decrease in nanohardness.

Despite the observed dislocations, the nanomechanical properties of copper are not significantly affected, likely due to its ability to accommodate stress through plastic deformation. The values for the Cu band are recorded as 215 ± 56 GPa for nanoindentation modulus and 4.3 ± 1.1 GPa for nanohardness, a 10% decrease in mechanical properties. Tungsten, with its robust thermal and chemical properties, does not show any change in nanomechanical properties after the tempering heat treatment, indicating its stability under such conditions.

5. Conclusions

- The microstructural examination demonstrated that the joint's overall microstructure remains largely unchanged following tempering, indicating that the tempering parameters were not intense enough to induce significant alterations. Stress relief at the joint interface occurred during tempering, resulting in reduced nanomechanical properties across various materials and phases within the joint.
- Despite heat treatment, critical precipitates unique to EUROFER, such as various MX precipitates of V and Ta, remained unaffected, with slightly enlarged grain sizes observed farther from the joint. This underscores EUROFER's resilience during tempering.
- While overall mechanical properties decreased post-tempering, the diffusion phase at the tungsten interface retained its high mechanical strength, indicating its robust nature. However, EUROFER experienced notable decreases in nanomechanical properties, highlighting its importance in joint performance analysis.
- Although the diffusion phase and iron-rich phase at the tungsten interface maintained their distinct characteristics after tempering, enhancements in diffusion processes were evident, notably in copper elements penetrating the diffusion phase.
- Copper's nanomechanical properties remained largely unaffected by tempering, indicating its capacity for stress accommodation through plastic deformation. Similarly, tungsten's properties remained stable under thermal treatment.
- Understanding these microstructural changes and their impact on mechanical properties is crucial for predicting material performance in fusion reactors and high-stress environments. Design considerations must account for the decrease in EUROFER's hardness and modulus post-tempering to ensure joint longevity and reliability.

CRediT authorship contribution statement

I. Izaguirre: Writing – original draft, Visualization, Validation, Methodology, Formal analysis, Data curation. **M. Roldán:** Writing – original draft, Visualization, Validation, Investigation, Formal analysis, Data curation. **J. de Prado:** Writing – original draft, Visualization, Validation, Investigation, Formal analysis, Data curation. **V. Bonache:** Writing – original draft, Visualization, Validation, Investigation, Formal analysis, Conceptualization. **M. Sánchez:** Writing – review & editing, Validation, Supervision, Resources, Project administration, Investigation, Funding acquisition, Conceptualization. **A. Ureña:** Writing – review & editing, Validation, Supervision, Resources, Project administration, Funding acquisition, Formal analysis.

Declaration of competing interest

The authors declare the following financial interests/personal relationships which may be considered as potential competing interests:

Ignacio Izaguirre reports financial support was provided by European Consortium for the Development of Fusion Energy. If there are other authors, they declare that they have no known competing financial interests or personal relationships that could have appeared to influence the work reported in this paper.

Data availability

Data will be made available on request.

Acknowledgements

This work has been carried out within the framework of the EUROfusion Consortium, funded by the European Union via the Euratom Research and Training Programme (grant agreement no. 10105220—EUROfusion). Views and opinions expressed are however those of the author(s) only and do not necessarily reflect those of the European Union or the European Commission. Neither the European Union nor the European Commission can be held responsible for them. The authors would also like to acknowledge the Community of Madrid in the framework of the Multiannual Agreement with the Rey Juan Carlos University in line of action 1, "Encouragement of Young PhD student's investigation" Project Ref. M 2168 Acronym DARUCEF. The authors acknowledge the use of instrumentation and the technical advice provided by the National Facility ELECMI ICTS, node "Laboratorio de Microscopías Avanzadas" at the University of Zaragoza.

References

[1] M. Richardson, M. Gorley, Y. Wang, G. Aiello, G. Pintsuk, E. Gaganidze, M. Richou, J. Henry, R. Vila, M. Rieth, Technology readiness assessment of materials for DEMO in-vessel applications, J. Nucl. Mater. 550 (2021) 152906, https://doi.org/10.1016/j.jnucmat.2021.152906.

[2] M. Kako, T. Tomizawa, J. Ge, X. Ruan, T. Nozawa, N. Yusa, The applicability of remote field eddy current testing to outer flaws on cooling tubes in the blanket of a fusion DEMO reactor, Fusion Eng. Des. 194 (2023) 113709, https://doi.org/10.1016/j.fusengdes.2023.113709.

[3] T.E.G. Nicholas, T.P. Davis, F. Federici, J. Leland, B.S. Patel, C. Vincent, S.H. Ward, Re-examining the role of nuclear fusion in a renewables-based energy mix, Energy Policy 149 (2021) 112043, https://doi.org/10.1016/j.enpol.2020.112043.

[4] J. Syblik, L. Vesely, S. Entler, J. Stepanek, V. Dostal, Analysis of supercritical CO2 Brayton power cycles in nuclear and fusion energy, Fusion Eng. Des. 146 (2019) 1520–1523, https://doi.org/10.1016/j.fusengdes.2019.02.119.

[5] E. Surrey, Engineering challenges for accelerated fusion demonstrators, Philos. Trans. R. Soc. A Math. Phys. Eng. Sci. 377 (2019), https://doi.org/10.1098/rsta.2017.0442.
[6] M. Bhuyan, H. Al Rashid, The effect of neon ion irradiation on tungsten for next generation fusion reactor, Mater. Today Proc. 65 (2022) 2698–2704, https://doi.org/10.1016/j.matpr.2022.05.343.
[7] Z. Wang, K. Zhao, W. Chen, X. Chen, L. Zhang, Phase transformation research of fusion reactor first wall material tungsten, Appl. Therm. Eng. 59 (2013) 498–503, https://doi.org/10.1016/j.applthermaleng.2013.06.017.
[8] T. Fu, K. Cui, Y. Zhang, J. Wang, F. Shen, L. Yu, J. Qie, X. Zhang, Oxidation protection of tungsten alloys for nuclear fusion applications: a comprehensive review, J. Alloys Compd. 884 (2021) 161057, https://doi.org/10.1016/j.jallcom.2021.161057.
[9] T. Echániz, I.G. de Arrieta, A. Gil-Muñoz, J. Fernández-Pereda, R. Fuente, M. Klimenkov, G.A. López, Infrared emissivity of reduced-activation Eurofer 97 for fusion reactor applications, J. Nucl. Mater. 549 (2021), https://doi.org/10.1016/j.jnucmat.2021.152907.
[10] D. Kumar, J. Hargreaves, A. Bharj, A. Scorror, L.M. Harding, H. Dominguez-Andrade, R. Holmes, R. Burrows, H. Dawson, A.D. Warren, P.E.J. Flewitt, T. L. Martin, The effects of fusion reactor thermal transients on the microstructure of Eurofer-97 steel, J. Nucl. Mater. 554 (2021) 153084, https://doi.org/10.1016/j.jnucmat.2021.153084.
[11] K. Li, J. Shan, C. Wang, Z. Tian, The role of copper in microstructures and mechanical properties of laser-welded Fe-19Ni-3Mo-1.5Ti maraging steel joint, Mater. Sci. Eng. A 681 (2017) 41–49, https://doi.org/10.1016/j.msea.2016.10.039.
[12] S.A. Fabritsiev, A.S. Pokrovsky, Neutron irradiation induced high temperature embrittlement of pure copper, Plasma Devices Oper. 5 (1997) 133–141, https://doi.org/10.1080/10519999708228025.
[13] Y. Li, C. Chen, R. Yi, Y. Ouyang, Review: special brazing and soldering, J. Manuf. Process. 60 (2020) 608–635, https://doi.org/10.1016/j.jmapro.2020.10.049.
[14] X. Liu, Y. Han, J. Wei, G. Zu, Y. Zhao, W. Zhu, X. Ran, Effect of tempering temperature on microstructure and mechanical properties of a low carbon bainitic steel treated by quenching-partitioning-tempering (QPT) process, J. Mater. Res. Technol. 23 (2023) 911–918, https://doi.org/10.1016/j.jmrt.2023.01.061.
[15] M.J.R. Sandim, F.U. Farrão, V.B. Oliveira, E.H. Bredda, A.D. Santos, C.A.M. Dos Santos, H.R.Z. Sandim, Effect of tempering on the microstructure, electrical, and magnetic properties of Eurofer-97 steel, J. Nucl. Mater. 461 (2015) 265–270, https://doi.org/10.1016/j.jnucmat.2015.03.020.
[16] M. Rieth, M. Schirra, A. Falkenstein, P. Graf, S. Heger, H. Kempe, R. Lindau, H. Zimmermann, EUROFER 97 tensile, charpy, creep and structural tests, Meas. J. Int. Meas. Confed. 140 (2003) 142–150.
[17] A.J. Santos, B. Lacroix, F. Maudet, F. Paumier, S. Hurand, C. Dupeyrat, V.J. Gómez, D.L. Huffaker, T. Girardeau, R. García, F.M. Morales, Application of advanced (S)TEM methods for the study of nanostructured porous functional surfaces: a few working examples, Mater. Charact. (2022) 185, https://doi.org/10.1016/j.matchar.2022.111741.
[18] M. Klimenkov, R. Lindau, E. Materna-Morris, A. Möslang, TEM characterization of precipitates in EUROFER 97, Prog. Nucl. Energy 57 (2012) 8–13, https://doi.org/10.1016/j.pnucene.2011.10.006.
[19] H. Wang, A. Kostka, W.E. Goosen, G. Eggeler, J.E. Westraadt, TEM replica analysis of particle phases in a tempered martensite ferritic Cr steel after long term creep, Mater. Charact. 181 (2021) 111396, https://doi.org/10.1016/j.matchar.2021.111396.
[20] P. Fernández, J. Hoffmann, M. Rieth, M. Roldán, A. Gómez-Herrero, TEM characterization on new 9% Cr advanced steels thermomechanical treated after tempering, J. Nucl. Mater. 500 (2018) 1–10, https://doi.org/10.1016/j.jnucmat.2017.12.025.
[21] J. de Prado, M. Roldán, M. Sánchez, V. Bonache, J. Rams, A. Ureña, Interfacial characterization by TEM and nanoindentation of W-Eurofer brazed joints for the first wall component of the DEMO fusion reactor, Mater. Charact. 142 (2018) 162–169, https://doi.org/10.1016/j.matchar.2018.05.035.
[22] Y. Yang, Y. Bi, J. Su, Z. Luo, Precipitate characteristic and nanoindentation analysis of resistance element welded DP780 steel and 6061 aluminum alloy joint, Mater. Lett. 347 (2023) 134571, https://doi.org/10.1016/j.matlet.2023.134571.
[23] G. Zengliang, S. Yuxuan, P. Zhouxin, C. Jianan, M. Yi, Nanoindentation investigation on the creep behavior of P92 steel weld joint after creep-fatigue loading, Int. J. Fatigue 134 (2020), https://doi.org/10.1016/j.ijfatigue.2020.105506.
[24] I. Izaguirre, M. Roldán, J. de Prado, V. Bonache, M. Sánchez, A. Ureña, S/TEM examination and nanomechanical response of W-Eurofer joints brazed with Cu interlayers, Nucl. Mater. Energy 31 (2022) 101155, https://doi.org/10.1016/j.nme.2022.101155.
[25] K. Mergia, N. Boukos, Structural, thermal, electrical and magnetic properties of Eurofer 97 steel, J. Nucl. Mater. 373 (2008) 1–8, https://doi.org/10.1016/j.jnucmat.2007.03.267.
[26] J. de Prado, M. Sánchez, M.V. Utrilla, M.D. López, A. Ureña, Study of a novel brazing process for W-W joints in fusion applications, Mater. Des. 112 (2016) 117–123, https://doi.org/10.1016/j.matdes.2016.09.067.
[27] H. Fredriksson, K. Hansson, A. Olsson, On the mechanism of liquid copper penetration into iron grain boundaries, Scand. J. Metall. 30 (2001) 41–50, https://doi.org/10.1034/j.1600-0692.2001.d01-36.x.
[28] ASM International, Alloy phase diagram, 1989. 10.1007/BF02881433.
[29] I. Ghamarian, P. Samimi, A. Telang, V.K. Vasudevan, P.C. Collins, Characterization of the near-surface nanocrystalline microstructure of ultrasonically treated Ti-6Al-4V using ASTAR^{TM}/precession electron diffraction technique, Mater. Sci. Eng. A 688 (2017) 524–531, https://doi.org/10.1016/j.msea.2017.02.029.
[30] J. Liu, S. Lozano-Perez, A.J. Wilkinson, C.R.M. Grovenor, On the depth resolution of transmission Kikuchi diffraction (TKD) analysis, Ultramicroscopy 205 (2019) 5–12, https://doi.org/10.1016/j.ultramic.2019.06.003.
[31] E.F. Rauch, J. Portillo, S. Nicolopoulos, D. Bultreys, S. Rouvimov, P. Moeck, Automated nanocrystal orientation and phase mapping in the transmission electron microscope on the basis of precession electron diffraction, Z. Kristallogr. 225 (2010) 103–109, https://doi.org/10.1524/zkri.2010.1205.
[32] R.L. Klueh, D.J. Alexander, E.A. Kenik, Development of low-chromium, chromium-tungsten steels for fusion, J. Nucl. Mater. 227 (1995) 11–23, https://doi.org/10.1016/0022-3115(95)00143-3.
[33] O. Prat, J. García, D. Rojas, J.P. Sanhueza, C. Camurri, Study of nucleation, growth and coarsening of precipitates in a novel 9%Cr heat resistant steel: experimental and modeling, Mater. Chem. Phys. 143 (2014) 754–764, https://doi.org/10.1016/j.matchemphys.2013.10.010.
[34] P. Anil Kumar, J. Vanaja, G.V. Prasad Reddy, G.V.S. Nageswara Rao, Effect of thermomechanical treatment and tempering temperature on microstructure and tensile properties of India specific reduced activation ferritic martensitic steel, J. Nucl. Mater. 574 (2023) 154186, https://doi.org/10.1016/j.jnucmat.2022.154186.
[35] M. Li, J.H. You, Design options to mitigate deep cracking of tungsten armor, Fusion Eng. Des. 124 (2017) 468–472, https://doi.org/10.1016/j.fusengdes.2017.01.015.
[36] Z. Deli, W. Xingli, G. Zongxiao, L. Yang, L. Ying, L. Weibing, Y. Chunyan, W. Fan, H. Jianjun, Performance and damage behaviors of detonation sprayed W/Fe/steel coatings under transient high heat fluxes, J. Nucl. Mater. 589 (2024) 154840, https://doi.org/10.1016/j.jnucmat.2023.154840.
[37] K.D. Zilnyk, P.A. Suzuki, H.R.Z. Sandim, Subtle microstructural changes during prolonged annealing of ODS-Eurofer steel, Nucl. Mater. Energy 35 (2023) 101450, https://doi.org/10.1016/j.nme.2023.101450.
[38] J. Fu, T.P. Davis, A. Kumar, I.M. Richardson, M.J.M. Hermans, Characterisation of the influence of vanadium and tantalum on yttrium-based nano-oxides in ODS Eurofer steel, Mater. Charact. 175 (2021), https://doi.org/10.1016/j.matchar.2021.111072.